Preprint Title Amorphized Length and Variability in Phase Change Memory Line Cells

Authors Nafisa Noor, Sadid Muneer, Raihan S. Khan, Anna Gorbenko and Helena Silva

Publication Date 07 Mai 2020

Article Type Full Research Paper

ORCID® iDs Nafisa Noor - https://orcid.org/0000-0002-8559-2425; Anna Gorbenko - https://orcid.org/0000-0002-9850-7912; Helena Silva - https://orcid.org/0000-0001-6356-5402

Amorphized Length and Variability in Phase Change Memory Line Cells

Nafisa Noor*[1,a)], Sadid Muneer[2,a)], Raihan Sayeed Khan[3], Anna Gorbenko[3], and Helena Silva[3]

Address: [1]Department of Electrical and Computer Engineering at North South University, Dhaka, Bangladesh

[2]Department of Electrical and Electronic Engineering at United International University, Dhaka, Bangladesh

[3]Department of Electrical and Computer Engineering at University of Connecticut, Storrs, CT-06269, USA

[a)] This research was performed while Nafisa Noor and Sadid Muneer were with the Department of Electrical and Computer Engineering at the University of Connecticut, Storrs, CT-06269, USA

* Nafisa Noor. Email: nafisa.noor@uconn.edu

* Corresponding author

Abstract

The dimensions of amorphized regions in phase-change memory cells are critical parameters to design devices for different applications but are difficult to determine by direct imaging. In this work, the length of amorphized regions in multiple, identical $Ge_2Sb_2Te_5$ (GST) line cells was extracted from electrical measurements. After each cell was programmed to an amorphous state, a sequence of increasing amplitude post-reset voltage pulses separated by low-amplitude read DC-sweeps was applied. When a sufficient amplitude post-reset voltage pulse was applied to a given cell, the measured current and the post-pulse resistance increased drastically, indicating the cell re-amorphized after threshold switching, melting, and quenching. The amorphized length was calculated using the measured voltage at which threshold switching took place and the expected drifted threshold field at that time. The measured threshold voltages, hence, the extracted amorphized lengths, generally increase linearly with the programmed resistance levels, but significant variability arises from the intrinsic uniqueness in the crystallization and amorphization processes in these devices. For example, cells programmed to ~50 MΩ amorphous resistance show threshold voltages of ~5-7 V, corresponding to amorphized lengths of ~240-360 nm. This unpredictable programming feature in phase-change memory devices can be utilized in hardware security applications.

Keywords

Amorphous materials, drift, electrical breakdown, electrical resistivity, phase change memory, pulse measurement, stochastic processes, threshold switching.

Introduction

Phase change memory (PCM) is an emerging non-volatile memory technology with high endurance, high speed, and good scalability. PCM relies on the change in phase of a nano-scale volume of a chalcogenide material sandwiched between two electrodes. The phase of the material can be switched between the high resistivity (amorphous or reset) and the low resistivity (crystalline or set) states by appropriate electrical pulses. The amorphization or reset process in PCM is achieved with a short and abrupt electrical pulse which melt-quenches the active region [1]. Nanoscale PCM devices exhibit significant cell-to-cell and cycle-to-cycle programming variability due to the intrinsic randomness in the crystallization and amorphization processes, in addition to any fabrication process variations. This probabilistic programming feature in PCM is recently being considered for several applications in hardware security, such as physical unclonable functions or true random number generators [2–8]. It is critical to characterize the physical factors contributing to the observed variability for conclusive understanding and proper utilization of this feature for these hardware security primitives. An essential physical parameter contributing to the programming variability is the random location and dimensions of different phases formed in the cell. The amorphous and crystalline regions in PCM devices can be distinguished by transmission electron microscopy (TEM) imaging [9], but this is a difficult and time-consuming process, and the sample preparation and imaging processes themselves may disturb the state of the material [10,11]. Hence, TEM becomes impractical for variability analysis using a large number of devices.

In this study, the lengths of the amorphized regions are calculated using electrical measurements on twenty-five $Ge_2Sb_2Te_5$ (GST-225) PCM line cells of very similar dimensions. The crystalline PCM line cells were first amorphized with a reset pulse. Then a sequence of post-reset pulses was applied, with gradually increasing amplitudes. The cells were read after each pulse. When the applied post-reset pulse amplitude was high enough, a significant increase

in the measured current and post-pulse cell resistance was observed, indicating re-amorphization after threshold switching, melting, and subsequent quenching, as inferred from the measurements and SPICE circuit simulation results. The measured threshold voltage, and the drifted threshold field at that time are used to extract the amorphized length (Figure 1).

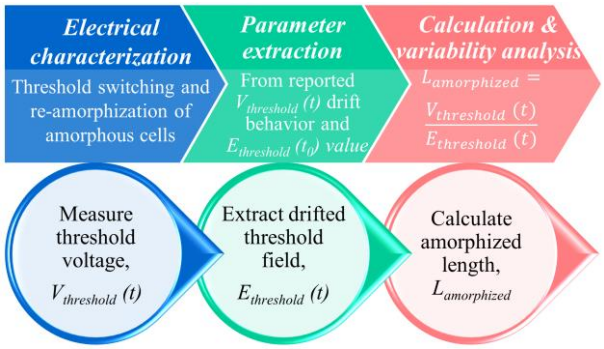

Figure 1: (a) Schematic of the procedure used in this work for extraction of amorphized length in phase-change memory line cells.

Threshold Switching in PCM

Threshold switching is defined by a sudden and reversible physical process in amorphous chalcogenides that accompanies a sharp decrease in resistance. Various models were presented in the 1970s to explain the threshold switching process; some of these models indicated pure thermal effects [12], some referred to pure electrical effects [13], and others pointed to a combination of both [14]. The argument was settled for decades with the dominance of the electrical model but then re-ignited in the last decade by the difficulties in understanding threshold switching in nanoscale PCM cells. Among the several new explanations based on electrical [15–19] and thermally assisted [20] effects, the electrical models are again prevailing, even though the specific mechanisms are expected to depend on the device geometry and dimensions [20].

According to the current understanding, threshold switching is initiated by electrical breakdown due to impact ionization, a purely electrical effect. The following sharp increase in current is ascribed to thermal runaway, i.e. the decrease in resistivity with increasing temperature that leads to further heating [18]. In this work, we use this model to interpret our measurement results.

Krebs et al. measured the threshold field of 56 V/μm for as-deposited GST amorphous bridge cells by measuring the threshold voltages of various known dimensions and concluded that threshold field is a material-dependent physical parameter, whereas, the specific threshold voltage depends on the device geometry [18]. As-deposited amorphous cells of known dimensions were used in Krebs' measurements, instead of the melt-quenched ones, to avoid the difficulty in determining the dimensions of the amorphized regions, but the drift time since deposition, which is a critical parameter, is difficult to extract. Since threshold voltage, $V_{threshold}\ (t)$ drifts upward in time [21], an effective threshold field, $E_{threshold}\ (t)$ is also expected to drift similarly, while the amorphized length, $L_{amorphized}$ is expected to remain the same over time, despite structural relaxation [22] or other physical processes that may occur in the amorphous volume below the glass transition:

$$E_{threshold}\ (t) = \frac{V_{threshold}\ (t)}{L_{amorphized}} \tag{1}$$

Lankhorst et al. measured a threshold field of 30-40 V/μm from melt-quenched GST devices at ~100 ns after amorphization [23]. Based on this known elapsed time after amorphization, t_0 and the threshold field at t_0, $E_{threshold}\ (t_0)$, it is possible to extract the threshold field $E_{threshold}\ (t)$ at the elapsed time between amorphization and the time when $V_{threshold}\ (t)$ was measured, t using the logarithmic trend of threshold voltage drift and the room temperature threshold voltage drift co-efficient, γ of 0.02 reported by Karpov et al. [21]:

$$\frac{V_{threshold}(t) - V_{threshold}(t_0)}{V_{threshold}(t_0)} = \gamma ln\left(\frac{t}{t_0}\right) \tag{2}$$

$$\frac{E_{threshold}(t) - E_{threshold}(t_0)}{E_{threshold}(t_0)} = \gamma ln\left(\frac{t}{t_0}\right) \quad (3)$$

In this work, we have used $E_{threshold}\ (t_0)$ of 35±5 V/μm calculated by Lankhorst et al. at t_0 ~ 100 ns after amorphization for melt-quenched amorphous line cells to obtain $E_{threshold}\ (t)$ at different measured times *t*, on different cells programmed to similar amorphous resistance using equation (3) and γ of 0.02, to calculate $L_{amorphized}$ and the associated variability. It is important to note that the term 'electrical breakdown' here refers to the reversible threshold switching process and not to the permanent and detrimental electrical breakdown failure that occurs in any dielectric.

Fabrication and Electrical Characterization

The GST-225 line cells used for this study were on silicon dioxide (SiO_2), had bottom metal contact pads (tungsten with Ti/TiN liner), and were capped by silicon nitride [24]. All cells were ~130 nm in width, W_{GST}, ~470 nm in length between the metal contacts, L_{GST}, and ~50 nm in thickness, t_{GST} (example scanning electron microscopy or SEM image in inset, Figure 2a). The as-fabricated cells were annealed in a Janis ST-500-UHT probe station at a pressure of ~1 mTorr at 675 K for 10 minutes to reach the stable hexagonal close packed or *hcp* crystalline phase (annealing profile shown in Figure 2a).

The electrical measurements were performed after cooling to room temperature. Electrical pulses, generated by an arbitrary function generator (Tektronix AFG 3102), were applied to the cells; a series load resistor of 5.1 kΩ was used to limit the current. The experimental circuit schematic is shown in Figure 2b. The experimental circuit was terminated through a digital oscilloscope (Tektronix DPO 4104) using two termination resistors of 50 Ω connected to channel 3 and 4. The applied voltage was monitored with Channel 1 of the oscilloscope and the voltage across the parallel combination of two 50 Ω resistors was monitored with channel 3 and 4 to determine the current through the cell. A semiconductor parameter analyzer (Agilent

4156C) was used for low-voltage read operations with a DC voltage sweep between −0.1 to +0.1 V for all resistance levels. A relay circuit, controlled by an Arduino Mega 2560 card, was used to switch between the reading and programming sequences of the measurements.

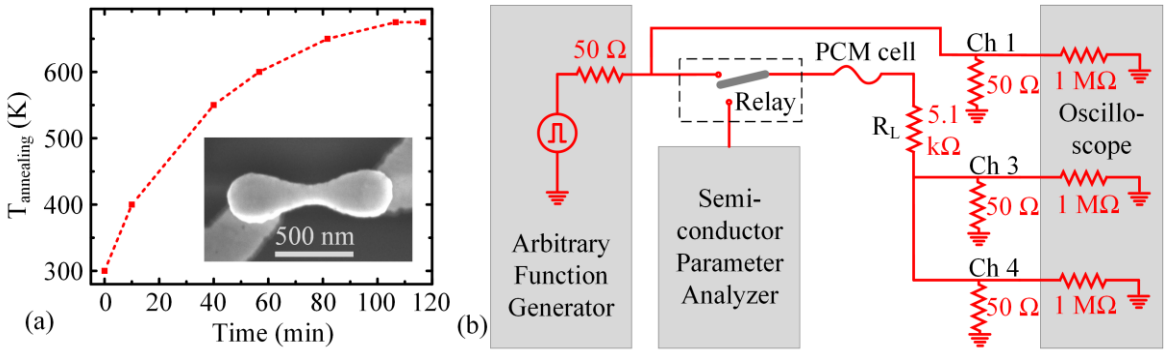

Figure 2: (a) Temperature ramp used for annealing as-fabricated amorphous devices to *hcp* phase, with a constant 675 K for the last 10 minutes. Inset shows the SEM image of an untested annealed GST line cell, with metal-to-metal L_{GST} ~470 nm, W_{GST} ~130 nm, and t_{GST} ~50 nm. (b) Electrical measurement setup.

Twenty-five identical *hcp* line cells with similar initial crystalline resistance values ($R_{crystalline}$) were amorphized to similar programmed resistance level ($R_{programmed}$) of ~10^7 Ω with a comparatively narrow distribution, so that the variations in initial $R_{programmed}$ do not greatly affect the extraction of $L_{amorphized}$. Table 1 shows the statistical distributions of the $R_{crystalline}$ and $R_{programmed}$ values for the 25 measured GST cells.

Table 1: Statistical Distribution of Cell Resistance. Minimum, maximum, and median of the crystalline and programmed resistance values ($R_{crystalline}$ and $R_{programmed}$) of the 25 measured GST cells (L_{GST} ~470 nm, W_{GST} ~130 nm, and t_{GST} ~50 nm).

Cell resistance	Minimum resistance	Maximum resistance	Median
$R_{crystalline}$	267 Ω	3162 Ω	522 Ω
$R_{programmed}$	8 MΩ	65 MΩ	28 MΩ

Due to intrinsic programming variability and process variations observed from cell to cell, the number(s) and the amplitude(s) of the applied voltage pulses to reach $R_{programmed}$ of ~10^7 Ω varied slightly [7,8]. The applied voltage amplitude required for this "initial reset" varied between ~2 and ~2.5 V whereas the number of pulses varied between 1 and 10. All amorphization voltage pulses were rectangular with a duration $t_{duration}$ of ~200 ns and rise and fall times t_{rise} = t_{fall} of ~25 ns. Once the cells reached this initial reset condition, a sequence of rectangular "post-reset pulses", with gradually increasing amplitudes (0.4 V to 10 V with a 0.1 V increment), and same $t_{duration}$, t_{rise}, and t_{fall} as used in the initial reset step, were applied. Low-voltage DC sweep read operations were performed before and after each applied pulse. Figure 3 shows the schematic of the measurement sequences.

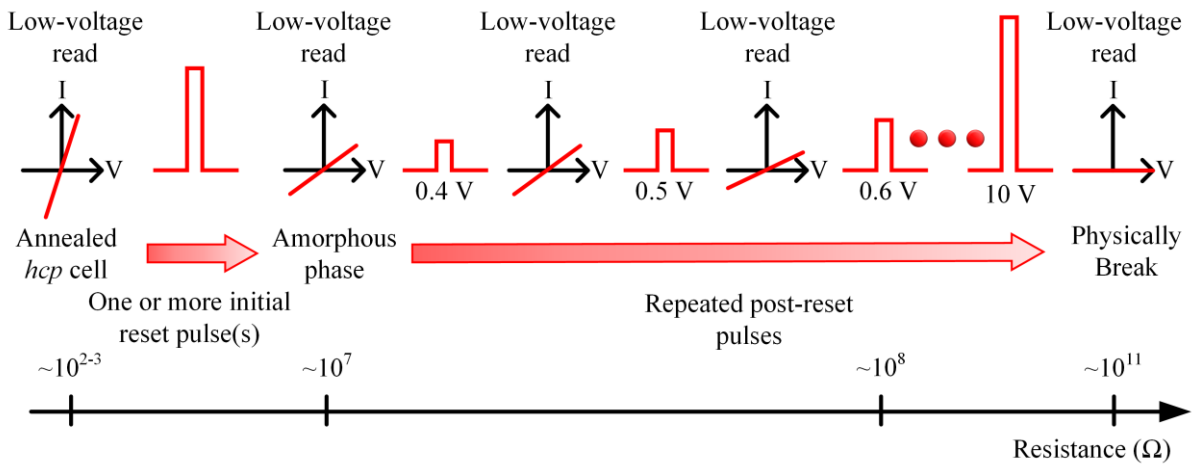

Figure 3: Measurement sequence. One or more pulses were applied to initially reset the *hcp* cells. Then a sequence of pulses with increasing amplitude (from 0.4 to 10 V in 0.1 V increment) were applied until further re-amorphization and eventually physical breaking occurred with loss of electrical connection. Low voltage read operations were performed before and after each applied pulse.

Results

(a) Re-amorphization of a single wire – measurements:

An example of the re-amorphization procedure on an initially amorphized cell is shown in Figure 4a with $R_{programmed}$ plotted as a function of the applied voltage at channel 1, $V_{ch1} = V_{post\text{-}reset}$. This cell was initially amorphized at 7.5 MΩ, with a certain amorphized length $L_{amorphized(1)}$. A schematic of the possible phase distribution in the cell after the initial reset is shown in Figure 5a. The amorphous cell started to show the usual upward resistance drift [25], which was unaffected by the early lower $V_{post\text{-}reset}$ pulses. After a $V_{post\text{-}reset}$ of 1.9 V was applied, $R_{programmed}$ drastically increased from the drifted amorphous resistance value of 10.55 MΩ to 48.05 MΩ (Figure 4a). The measured voltage at the channel 3 and 4 termination resistors, $V_{ch3,4}$ showed a sudden overshoot (green dotted line, Figure 4b - 2nd row). This $V_{ch3,4}$ amplitude was significantly higher than the barely noticeable $V_{ch3,4}$ magnitude for all the lower $V_{post\text{-}reset}$ amplitudes. An example of $V_{ch3,4}$ for $V_{post\text{-}reset}$ of 1 V is plotted in Figure 4b (2nd row - blue dashed line) to show the difference. Even though we monitored all waveforms, we only recorded a few to avoid adding extra elapsed time between amorphization and threshold switching.

The 1.9 V amplitude pulse caused a threshold switching, by means of the electrical breakdown of the already-existing insulating amorphous region of length $L_{amorphized(1)}$. Therefore, 1.9 V is the threshold voltage $V_{threshold(1)}$ for the breakdown of length $L_{amorphized(1)}$. The increased amorphous resistance indicates a larger effective length of the new amorphous region $L_{amorphized(2)}$ (Figure 5b), even though any voids formed would also alter the overall cell resistance. The cell resistance again started to drift upward and stayed unaffected by the next few post-reset pulses until the next threshold switching event at $V_{threshold(2)}$ of 8.2 V, of the amorphized region of length $L_{amorphized(2)}$. At this point, the wire itself broke physically, and the

electrical connection was lost, possibly due to void formation in the middle of the cell (Figure 5c).

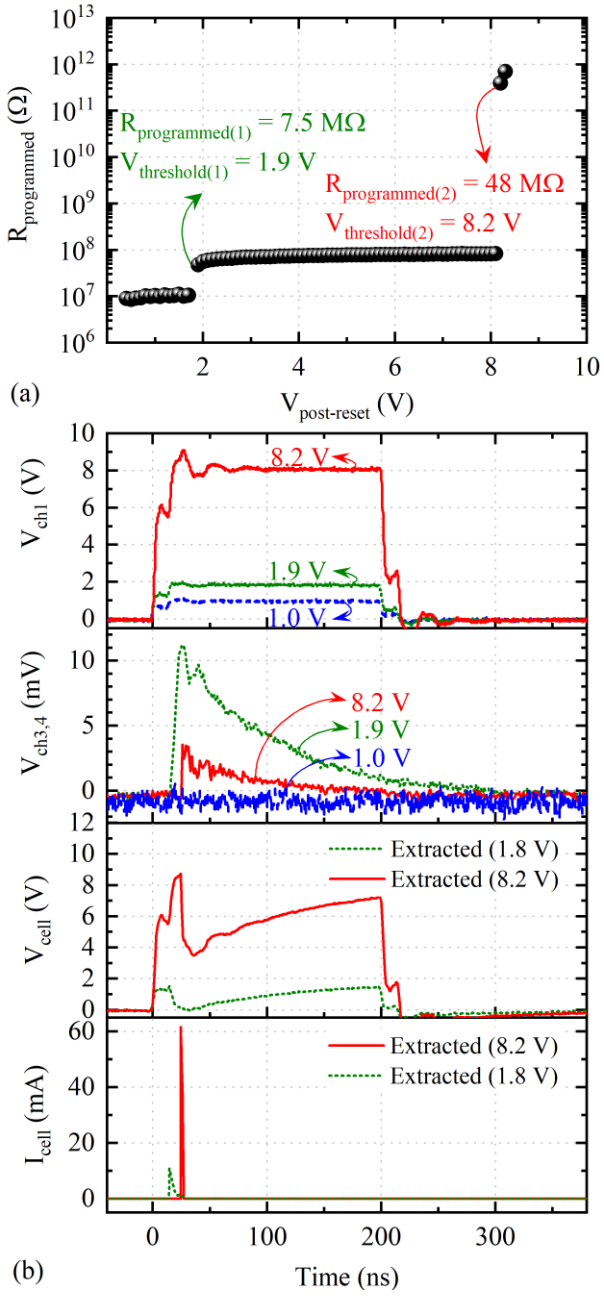

Figure 4: Repeated post-reset pulses of 200 ns duration and 0.4 to 10 V amplitudes (with an increment of 0.1 V) applied to an amorphous cell with L_{GST} of ~470 nm, W_{GST} of ~130 nm, and t_{GST} of ~50 nm, and initially programmed to ~7.5 MΩ.

(a) Evolution of $R_{programmed}$ as a function of post-reset pulse amplitude ($V_{post-reset}$).

(b) ***1st and 2nd rows*:** Example waveforms of applied voltage at channel 1 (V_{ch1}) and measured voltage at channel 3,4 ($V_{ch3,4}$) during an unsuccessful re-amorphization (blue dashed line), a successful re-amorphization at $V_{post\text{-}reset}$ of 1.9 V (green dotted line), and a breaking episode when electrical connections are lost at $V_{post\text{-}reset}$ of 8.2 V (red solid line).

***3rd and 4th rows*:** These voltage waveforms for the $V_{post\text{-}reset}$ of 1.9 and 8.2 V are inputted in the SPICE circuit simulations and the resulting cell voltage (V_{cell}) and current (I_{cell}) are extracted by modeling the experimental setup circuitry.

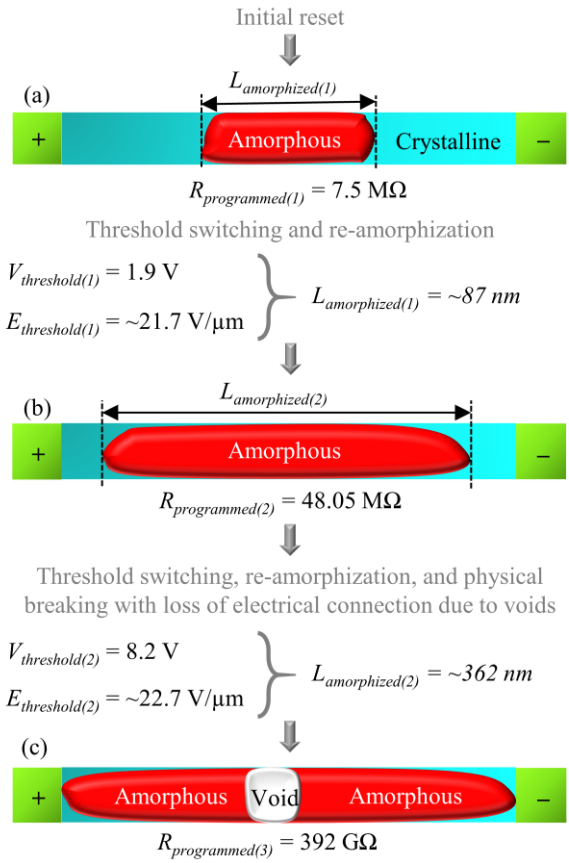

Figure 5: Schematic illustration of the calculation of amorphized length for the two post-reset re-amorphization episodes shown in Figure 4: (a) after initial reset, (b) after first re-amorphization at $V_{threshold(1)}$ of 1.9 V, (c) after second re-amorphization and physical breaking with loss of electrical connection at $V_{threshold(2)}$ of 8.2 V. Threshold voltages indicate the voltage at which the already existing amorphous region experienced electrical breakdown during threshold switching.

(b) Cell voltage and current extraction – circuit simulation:

A SPICE simulation was performed to extract the cell voltage and current (V_{cell} and I_{cell}) by inputting V_{ch1} and $V_{ch3,4}$ as voltage sources. Figure 6a illustrates the approximate circuit model of the experimental setup (shown in Figure 2b) with the following components:

1. Channel 1 termination resistance, R_{ch1} = 50 Ω.
2. Capacitance of coaxial cable to channel 1 termination, C_{ch1} = 110 pF.
3. Cell resistance, R_{cell}: values used for SPICE simulations are listed in Table 2.
4. Capacitance of probe arm to load resistor, C_{load} = 20 pF.
5. Load resistance, R_{load} = 5.1 kΩ.
6. Channel 3 and 4 termination resistance in parallel, $R_{ch3,4}$ = 50 || 50 Ω = 25 Ω.
7. Capacitance of coaxial cable to combined channel 3 and 4 terminations, $C_{ch3,4}$ = 110 pF.

Table 2: Cell Resistance R_{cell} values used for the two re-amorphization events in simulations.

Re-amorphization events	$R_{amorphous(before\text{-}pulse)}$, MΩ	R_{molten} (Ω)	$R_{amorphous(after\text{-}pulse)}$, MΩ
1st Re-amorphization (1.9 V)	10.55	140	48.05
2nd Re-amorphization (8.2 V)	82.66	140	392656.81

Table 3: Melting and re-amorphization instances, i.e., the switching times used for the two re-amorphization events in simulations.

Re-amorphization events	Melting instance, ns	Re-amorphization instance, ns
1st Re-amorphization (1.9 V)	14	28
2nd Re-amorphization (8.2 V)	24	26

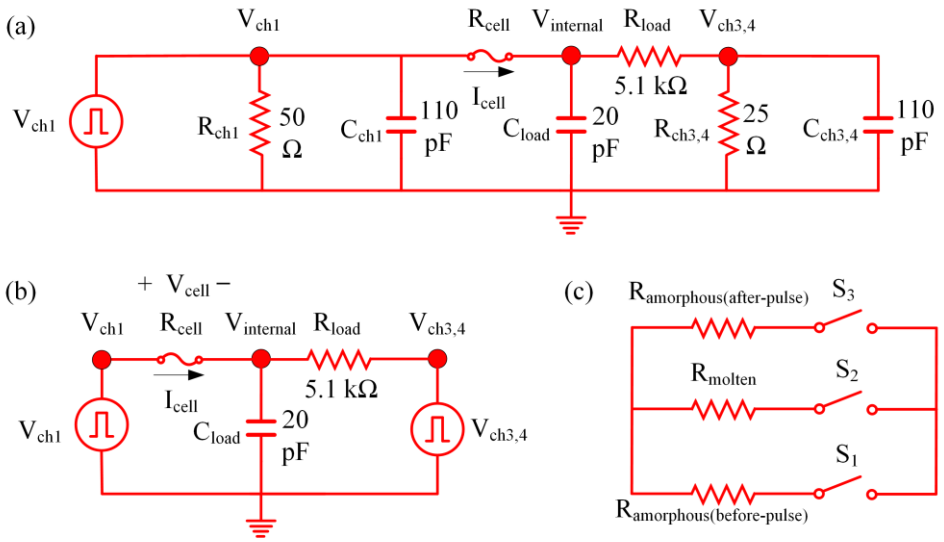

Figure 1: (a) Approximate circuit model of experimental setup with measured parasitic capacitance and resistance values. (b) Simplified circuit model simulated in SPICE with the measured V_{ch1} and $V_{ch3,4}$ waveforms. (c) Modeling of GST resistance switching with three switches in SPICE.

Figure 6b shows the simplified circuit model, in which the parasitic capacitances and termination resistances for both channel 1 and channel 3,4 are already taken into account with the measured V_{ch1} and $V_{ch3,4}$. R_{cell} is switched between the measured amorphous resistance before pulse $R_{amorphous(before\text{-}pulse)}$, a molten resistance R_{molten} of 140 Ω, and the measured amorphous resistance after pulse $R_{amorphous(after\text{-}pulse)}$ (Figure 6c) for the two re-amorphization events shown in Figure 4. The R_{molten} value is assumed to be 140 Ω for all simulations, which is slightly less than the *hcp* $R_{crystalline}$, since melting incorporates a drop in the GST resistivity [26]. Table 2 lists these different resistance values used for the circuit simulations.

Melting and re-amorphization of GST cell is simulated with three switches S_1, S_2, and S_3 that sequentially turn on and off to include the appropriate R_{cell} (Figure 6c). For both re-amorphization cases, the melting is assumed to take place when $V_{ch3,4}$ starts to rise and the re-amorphization is assumed to take place right after the peak of $V_{ch3,4}$. Table 3 lists the melting and re-amorphization instances for the two re-amorphization events used in simulations.

At the starting of the simulation, S_1 is closed while S_2 and S_3 are kept open to use $R_{amorphous(before\text{-}pulse)}$ as the starting R_{cell}. During melting, R_{cell} is switched from $R_{amorphous(before\text{-}pulse)}$ to R_{molten} by opening S_1 and closing S_2, with S_3 open. For re-amorphization, R_{cell} is switched from R_{molten} to $R_{amorphous(after\text{-}pulse)}$ by opening S_2 and closing S_3, with S_1 open.

For both re-amorphization events, the $V_{cell} \approx V_{ch1}$ at the beginning, when $R_{cell} \approx R_{amorphous(before\text{-}pulse)}$, since $R_{amorphous(before\text{-}pulse)} >> R_{load}$ and most of the applied V_{ch1} voltage is dropped across the cell. When melting occurs, the V_{cell} decreases and I_{cell} increases sharply, since $R_{molten} << R_{load}$. When quenching occurs, V_{cell} increases slowly again, since $R_{amorphous(after\text{-}pulse)} >> R_{load}$, and I_{cell} decreases sharply due to amorphization (Figure 4a – 3rd and 4th rows).

We note that I_{cell} for each of the re-amorphization events consists of a very sharp triangular current pulse (of ~15 ns duration and ~11 mA amplitude for the 1st re-amorphization and ~3 ns duration and ~62 mA amplitude for the 2nd event), which occurs during the rising edge of the V_{ch1}. The very sharp rising edges of I_{cell} for the two re-amorphization events can be attributed to the additional capacitive current contributions due to the parasitic capacitances present in the system and to the thermal runaway of amorphous GST, which also lead to a quick rise of the cell temperature and produce enough Joule heating to induce melting of the material [27]. The sharp falling edges of I_{cell} for the two re-amorphization events due to the discharge of parasitic capacitance can initiate quenching and block the conduction path resulting in re-amorphization [28].

(c) Re-amorphization of twenty-five wires – measurements:

We repeated the re-amorphization study on 25 cells and measured $V_{threshold}\,(t)$ values, which we plotted against the programmed resistance values measured at 10 s after amorphization ($R_{programmed}\,(10\ s)$) in Figure 7a. Cells with higher $R_{programmed}$ (17 out of 25 cells) physically broke after the first amorphization (i.e. initial reset) without any intermediate re-amorphization

episode and are plotted as spheres in Figure 7a. Cells that experienced one or more re-amorphization episode(s) are plotted as stars connected with dotted lines in Figure 7a.

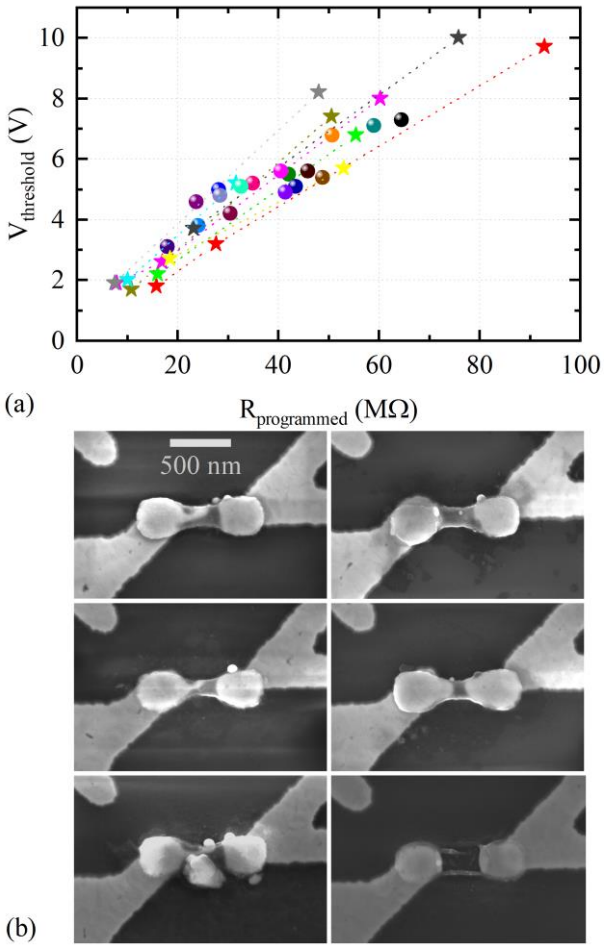

Figure 7: (a) $V_{threshold}$ *(t)* for 25 identical cells as a function of $R_{programmed}$. The data-points for different cells are plotted with different colors. Cells that demonstrated multiple re-amorphization events are plotted with stars connected with dotted lines (8 out of 25 cells) and the ones experiencing a the single re-amorphization event are plotted with spheres (17 out of 25 cells). (b) Example SEM images of 6 physically broken cells with lost connection show significant variability in the void formation, despite having similar dimension (L_{GST} ~470 nm, W_{GST} ~130 nm, and t_{GST} ~50 nm) and being programmed to similar initial $R_{programmed}$.

The loss of electrical connection in the wire was confirmed by post-pulse DC I-V characteristics and SEM imaging performed after the electrical characterization (Figure 7b). The extrapolated $E_{threshold}$ *(t)* (Figure 8a) and measured $V_{threshold}$ *(t)* (Figure 8b), both at a certain

time *t*, which is different for different measured cells, are used to calculate $L_{amorphized}$ (Figure 8c) using equation (1). Since $L_{amorphized}$ remains the same for a given amorphized region, it is only important to consistently extrapolate $E_{threshold}\ (t)$ at the time *t* when we measure $V_{threshold}\ (t)$.

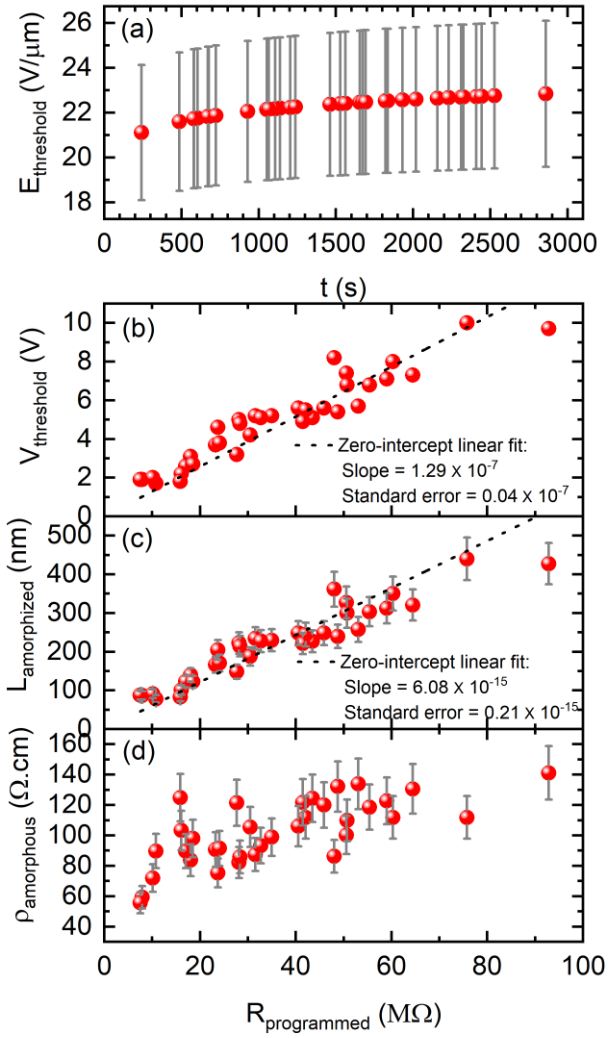

Figure 8: (a) Logarithmic upward drift of threshold field $E_{threshold}\ (t)$ [21] and the associated error from the reported value [23] as a function of elapsed time after amorphization *t*. (b) Measured threshold voltage $V_{threshold}\ (t)$ as a function of the measured $R_{programmed}$, (c) calculated $L_{amorphized}$ with the error propagated from the reported $E_{threshold}\ (t_0)$ as a function of the measured $R_{programmed}$, and (d) calculated $\rho_{amorphous}\ (10\ s)$ with the error propagated from the reported $E_{threshold}\ (t_0)$ as a function of the measured $R_{programmed}$.

We observed a linear relation between the measured $V_{threshold}\ (t)$ and $R_{programmed}$ (Figure 7 and Figure 8b), which in turn is linearly related with the calculated $L_{amorphized}$ with a moderate degree of variability (Figure 8c). The error in the reported $E_{threshold}\ (t_0)$ of ±5 V/µm is propagated in the extrapolated $E_{threshold}\ (t)$ and the calculated $L_{amorphized}$, plotted as the gray error bars in Figure 8, using the standard methods of propagation of uncertainties [29].

In addition to this variability, there was also cell-to-cell variability in the measured $V_{threshold}\ (t)$ value for a certain $R_{programmed}$ (Figure 7a) and this cell-to-cell variability is also propagated to the zero-intercept fitted expression for $L_{amorphized}$:

$$V_{threshold} = R_{programmed} \times (1.29 \pm 0.04)\ \frac{V}{10\ M\Omega} \tag{4}$$

$$L_{amorphized} = R_{programmed} \times (60.82 \pm 2.11)\ \frac{nm}{10\ M\Omega} \tag{5}$$

Equations (4) and (5) show that for an amorphous region programmed to 10 MΩ, a $V_{threshold}$ of 1.29 ± 0.04 V is required for threshold switching, indicating an $L_{amorphized}$ of 60.82 ± 2.11 nm. Besides process variations, these variations observed in $V_{threshold}\ (t)$ and $L_{amorphized}$ can be ascribed to:

- variations in the initial $R_{crystalline}$ values (shown in Table 1 for the 25 measured cells), due to the random arrangement of grains in the cells [30],
- variations in shape of the amorphous volumes within the dog-bone shaped line cell,
- slightly different numbers and amplitudes of the applied initial reset pulse(s), which might have amorphized the cell either with a single pulse or with multiple pulses in a more gradual manner [8],
- variations in reported $E_{threshold}\ (t_0)$ itself (35 ± 5 V/µm [23]),
- random arrangement of any voids created after every reset operation (Figure 7b) [31], and
- variable amorphous resistance drift [32] of different cells during the elapsed times between amorphization and threshold switching.

Assuming an ideal uniform cross-section of the amorphous regions, covering the entire cross-section area $A_{amorphous} = W_{GST} \times t_{GST}$ (W_{GST} ~130 nm, t_{GST} ~50 nm), the amorphous resistivity at ~10 s after amorphization, $\rho_{amorphous}\,(10\ s)$, can be calculated using the extracted $L_{amorphized}$ and the drifted $R_{programmed}\ (10\ s)$:

$$\rho_{amorphous}(10\ s) = \frac{W \times t}{\left(\frac{L_{amorphized}}{R_{programmed}\ (10\ s)}\right)} \tag{6}$$

$$= \frac{130 \times 10^{-9}\ m \times 50 \times 10^{-9}\ m}{(6.13 \pm 0.21) \times 10^{-15}\frac{m}{\Omega}} = 106.04\ \pm 3.58\ \Omega.\ cm$$

The calculated $\rho_{amorphous}\ (10\ s)$ is plotted as a function of the $R_{programmed}$ at 10 s in Figure 8d. The calculated $\rho_{amorphous}\ (10\ s)$ of ~ 106 Ω.cm, which is consistent with our earlier reported value of ~148 Ω.cm at ~60 s after amorphization obtained from line cells [24]. This close match validates the accuracy of the amorphized length estimation method used in this paper. It is important to note that the $\rho_{amorphous}\ (10\ s)$ calculation uses the extracted $L_{amorphized}$ vs. measured $R_{programmed}$ at 10 s values, measured under low-field (-0.1 to +0.1 V DC sweep) after the post-reset pulse was applied, hence $\rho_{amorphous}$ is a low-field resistivity calculation.

Conclusion

We propose a method to extract amorphized length in phase-change memory devices based on electrical measurements. We utilized this procedure to study the variability in amorphized lengths in 25 amorphized GST line cells of identical dimensions. Each cell is initially programmed to a similar amorphous resistance level (~ 8-65 MΩ) and then tested with a sequence of post-reset pulses of gradually increasing amplitude, separated by low-amplitude read DC sweeps. When the post-reset pulse amplitude is sufficient, a given cell undergoes threshold switching, melting and quenching and is re-amorphized, as inferred by the

measurement and circuit simulation results. The process is continued until the cell breaks to observe as many re-amorphization events as possible.

Each re-amorphization event is observed as a sudden increase in current during the pulse and a higher resistance after pulse, corresponding to a larger effective amorphized volume. The sharp increase in cell current is attributed to the parasitic capacitive current and thermal runaway in amorphous GST. The re-amorphization to increasingly higher resistance levels is also due to the sharp capacitive discharge current at the end of the post-reset pulse.

Using the measured threshold voltage, and assuming an effective drifted threshold field at that switching time, we extracted the length of the amorphized region that experienced threshold switching, for each re-amorphization event, and related it with its previous resistance level. We observe a generally linear relation, but with a significant spread, between the amorphized length and the programmed resistance. The amorphous resistivity calculated using the extracted amorphized length and the drifted programmed resistance is ~106 Ω.cm, within the range of previously reported values for melt-quenched GST, validating the accuracy of the amorphized length estimation method used in this paper.

The variability in the calculated amorphized lengths, based on the measured threshold voltages, can be attributed to different physical mechanisms such as the variable amorphous resistance drift and cycling history, the unique amorphous volumes formed, and different crystalline and amorphous initial conditions. SEM images of physically broken cells captured after the electrical measurements show the randomness in the distribution of voids formed during recurrent reset operations, indicating another important factor for the observed variability. Combining these different physical sources of intrinsic variability in cell-to-cell and cycle-to-cycle operations, PCM devices can offer a promising platform for hardware security primitives, in which numerous origins of variability is a well-desired feature.

Acknowledgment

N. N. performed the electrical measurements, SEM imaging, data analysis, and overall conception of the idea and writing of the manuscript. S. M. and R. S. K. automatized the electrical measurements. A. G., supported by U. S. National Science Foundation under research experience for undergraduate (REU) award ECCS 1150960, provided technical supports by reproducing some electrical measurements. H. S. supervised the overall work and worked on the preparation of the manuscript.

The facilities at UConn-Thermo Fisher Scientific Center at University of Connecticut are used for the scanning electron microscope (SEM) images. The devices are fabricated at IBM Watson Research Center under a joint study agreement with the University of Connecticut. We thank Dr. Faruk Dirisaglik, Dr. Adam Cywar, Dr. Chung Lam, and Dr. Yu Zhu for their support in device fabrication, and Professor Ali Gokirmak with the University of Connecticut for valuable discussions.

Funding

This research is funded by the multi-university research initiative (MURI) of Air Force Office of Scientific Research (AFOSR) under the grant FA9550-14-1-0351Z.

References

(1) Burr, G. W.; Breitwisch, M. J.; Franceschini, M.; Garetto, D.; Gopalakrishnan, K.; Jackson, B.; Kurdi, B.; Lam, C.; Lastras, L. A.; Padilla, A. *J. Vac. Sci. Technol. B* **2010**, *28*, 223. doi:10.1116/1.3301579

(2) Zhang, L.; Kong, Z. H.; Chang, C. H.; Cabrini, A.; Torelli, G. *IEEE Trans. Inf. Forensics Secur.* **2014**, *9* (6), 921–932. doi:10.1109/TIFS.2014.2315743

(3) Noor, N.; Silva, H. Phase Change Memory for Physical Unclonable Functions. In *Applications of Emerging Memory Technology*; Suri, M., Ed.; Springer Verlag: Singapore, 2020; Vol. 63, pp 59–91. doi:10.1007/978-981-13-8379-3_3

(4) Khan, R. S.; Noor, N.; Jin, C.; Scoggin, J.; Woods, Z.; Muneer, S.; Ciardullo, A.; Nguyen, P. H.; Gokirmak, A.; Dijk, M. van; Silva, H. Phase Change Memory and Its Applications in Hardware Security. In *Security Oppotunities in Nano Devices and Emerging Technologies*; Tehranipoor, M., Forte, D., Rose, G. S., Bhunia, S., Eds.; CRC Press: boca raton, FL, USA, 2017; pp 93–114

(5) Noor, N. Exploiting Phase Change Memory Nano-Device Properties for Hardware Security Applications. PhD Dissertation, Department of Electrical and Computer Engineering, University of Connecticut, Storrs, CT, USA, 2019

(6) Noor, N.; Muneer, S.; Khan, R. S.; Gokirmak, A.; Silva, H. Enhanced Reset Variability in Phase Change Memory for Hardware Security Applications. In *Bulletin of the American Physical Society*; American Physical Society (APS): Boston, MA, USA, 2019

(7) Noor, N.; Muneer, S.; Adnane, L.; Khan, R. S.; Gorbenko, A.; Dirisaglik, F.; Cywar, A.; Lam, C.; Zhu, Y.; Gokirmak, A.; Silva, H. Utilizing Programming Variability in Phase Change Memory Cells for Security. In *2017 Material Research Society (MRS) Fall Meeting & Exhibit*; Materials Research Society: Boston, MA, USA, 2017

(8) Noor, N.; Muneer, S.; Khan, R. S.; Gorbenko, A.; Adnane, L.; Kashem, M. T. Bin;

Scoggin, J.; Dirisaglik, F.; Cywar, A.; Gokirmak, A.; Silva, H. *IEEE Trans. Nanotechnol.* **2020**, *submitted*

(9) Santala, M. K.; Raoux, S.; Topuria, T.; Reed, B. W. *Thin Solid Films* **2014**, *571* (1), 39–44. doi:10.1016/j.tsf.2014.09.063

(10) Tripathi, S.; Janish, M.; Dirisaglik, F.; Cywar, A.; Zhu, Y.; Jungjohann, K.; Silva, H.; Carter, C. B. *Microsc. Microanal.* **2018**, *24* (S1), 1904–1905. doi:10.1017/S1431927618010000

(11) Tripathi, S.; Carter, C. B.; Jungjohann, K. L.; Janish, M.; Noor, N.; Kotula, P. G.; Pete, D. V; Silva, H. PCM Materials & Devices: In-Situ TEM Imaging. In *CINT User's Meeting*; Sandia National Lab: Albuquerque, NM, USA, 2018

(12) Warren, A. C. *IEEE Trans. Electron Devices* **1973**, *20* (2), 123–131. doi:10.1109/T-ED.1973.17618

(13) Adler, D.; Henisch, H. K.; Mott, S. N. *Rev. Mod. Phys.* **1978**, *50* (2), 209–220

(14) Owen, A. E.; Robertson, J. M. *IEEE Trans. Electron Devices* **1973**, *20* (2), 105–122. doi:10.1109/T-ED.1973.17617

(15) Ielmini, D.; Zhang, Y. *J. Appl. Phys.* **2007**, *102* (5). doi:10.1063/1.2773688

(16) Jacoboni, C.; Piccinini, E.; Buscemi, F.; Cappelli, A. *Solid. State. Electron.* **2013**, *84*, 90–95. doi:10.1016/J.SSE.2013.02.007

(17) Jandieri, K.; Rubel, O.; Baranovskii, S. D.; Reznik, A.; Rowlands, J. A.; Kasap, S. O. *Phys. Status Solidi Curr. Top. Solid State Phys.* **2008**, *5* (3), 796–799. doi:10.1002/pssc.200777565

(18) Krebs, D.; Raoux, S.; Rettner, C. T.; Burr, G. W.; Salinga, M.; Wuttig, M. *Appl. Phys. Lett.* **2009**, *95*, 82101

(19) Wimmer, M.; Salinga, M. *New J. Phys.* **2014**, *16* (11), 113044. doi:10.1088/1367-2630/16/11/113044

(20) Le Gallo, M.; Athmanathan, A.; Krebs, D.; Sebastian, A. *J. Appl. Phys.* **2016**, *119* (2).

doi:10.1063/1.4938532

(21) Karpov, I. V.; Mitra, M.; Kau, D.; Spadini, G.; Kryukov, Y. A.; Karpov, V. G. *J. Appl. Phys.* **2007**, *102* (12), 124503. doi:10.1063/1.2825650

(22) Ielmini, D.; Lavizzari, S.; Sharma, D.; Lacaita, A. L. Physical Interpretation, Modeling and Impact on Phase Change Memory (PCM) Reliability of Resistance Drift Due to Chalcogenide Structural Relaxation. In *2007 IEEE International Electron Devices Meeting (IEDM)*; IEEE: Washington, DC, USA, 2007; pp 939–942

(23) Lankhorst, M. H. R.; Ketelaars, B. W. S. M. M.; Wolters, R. A. M. *Nat. Mater.* **2005**, *4* (4), 347–352

(24) Dirisaglik, F. High-Temperature Electrical Characterization of Ge2Sb2Te5 Phase Change Memory Devices. Ph.D. dissertation, Dept. of Elec. & Comp. Engr., Univ. of Connecticut, Storrs, CT, USA, 2014

(25) Dirisaglik, F.; Bakan, G.; Jurado, Z.; Muneer, S.; Akbulut, M.; Rarey, J.; Sullivan, L.; Wennberg, M.; King, A.; Zhang, L.; Nowak, R.; Lam, C.; Silva, H.; Gokirmak, A. *Nanoscale* **2015**, *7* (40), 16625–16630. doi:10.1039/C5NR05512A

(26) Adnane, L.; Dirisaglik, F.; Cywar, A.; Cil, K.; Zhu, Y.; Lam, C.; Anwar, A. F. M.; Gokirmak, A.; Silva, H. *J. Appl. Phys.* **2017**, *122* (12), 125104. doi:10.1063/1.4996218

(27) Bakan, G.; Cywar, A.; Silva, H.; Gokirmak, A. *Appl. Phys. Lett.* **2009**, *94* (25), 251910. doi:10.1063/1.3159877

(28) Ielmini, D.; Mantegazza, D.; Lacaita, A. L.; Pirovano, A.; Pellizzer, F. *IEEE Electron Device Lett.* **2005**, *26* (11), 799–801. doi:10.1109/LED.2005.857719

(29) Taylor, J. R. *An Introduction to Error Analysis : The Study of Uncertainties in Physical Measurements*, 2nd ed.; University Science Books: New York, NY, 1997

(30) Woods, Z.; Scoggin, J.; Cywar, A.; Adnane, L.; Gokirmak, A. *IEEE Trans. Electron Devices* **2017**, *64* (11), 4472–4478. doi:10.1109/TED.2017.2745500

(31) Cywar, A. D. Melting and Crystallization of Si and Ge2Sb2Te5 Nanostructures. Ph.D.

dissertation, Dept. of Elec. & Comp. Engr., Univ. of Connecticut, Storrs, CT, USA, 2016

(32) Boniardi, M.; Ielmini, D.; Lavizzari, S.; Lacaita, A. L.; Redaelli, A.; Pirovano, A. *IEEE Trans. Electron Devices* **2010**, *57* (10), 2690–2696. doi:10.1109/TED.2010.2058771